Advanced Energy Materials

ADVANCED ENERGY MATERIALS
www.advenergymat.de

RESEARCH ARTICLE OPEN ACCESS

Supramolecularly Directed Confined Crystallization of Lamellar Carbon Nitride for Efficient Photocatalytic Hydrogen Generation

Nithinraj Panangattu Dharmarajan[1] | Mohammed Fawaz[1] | Jae-Hun Yang[1] | Matej Huš[2] | Xuan Minh Chau Ta[3] | Ayona K. Jose[1] | Vibin Perumalsamy[1] | Aathira M. Sadanandan[1] | CI Sathish[1] | Blaž Likozar[2] | Byoung-Hwa Lee[4] | Chung-Hwan Jeon[4] | Antonio Tricoli[3] | Ajayan Vinu[1]

[1]Global Innovative Centre for Advanced Nanomaterials, College of Engineering, Science and Environment, The University of Newcastle, New South Wales, Australia | [2]Department of Catalysis and Chemical Reaction Engineering, National Institute of Chemistry, Ljubljana, Slovenia | [3]Nanotechnology Research Laboratory, Faculty of Engineering, University of Sydney, New South Wales, Australia | [4]Pusan Clean Energy Research Institute, School of Mechanical Engineering, Pusan National University, Busan, South Korea

Correspondence: Mohammed Fawaz (mohammedfawaz.palakkatalihassan@newcastle.edu.au) | Jae-Hun Yang (jaehun.yang@newcastle.edu.au) | Ajayan Vinu (ajayan.vinu@newcastle.edu.au)

Received: 8 February 2026 | **Revised:** 8 February 2026 | **Accepted:** 24 March 2026

Keywords: carbon nitride | hydrogen production | photocatalysis | supramolecular self-assembly

ABSTRACT

Sustainable hydrogen generation through water splitting is key to realizing a future hydrogen economy. In this study, we achieved molecular-level control over self-assembled supramolecular complexes of cyanuric acid and 3-amino 1,2,4 triazole (AT) monomers. This was coupled with molten-salt-assisted thermal polymerization in a eutectic mixture of lithium chloride and potassium chloride to synthesize a crystalline carbon nitride with a high surface area and specific crystal structure. Conventional eutectic molten salt synthesis typically yields a mixture of poly (heptazine imide) (PHI) and poly (triazine imide) (PTI) phases. In contrast, the supramolecular complex-derived approach confines crystal growth through molecular alignment, resulting in the formation of pure PHI phase. To date, the advantages of supramolecular complex precursors have been largely limited to their enhanced surface area and unique morphologies. Here, we demonstrate that this strategy can be extended to direct crystal growth toward a specific phase. This insight enables the synthesis of phase-pure crystalline carbon nitride at low temperatures, even in eutectic molten salt systems, which was not possible previously. The supramolecular complex in LiCl/KCl eutectic mixture suppresses PTI formation and promotes Li- and K-stabilized PHI, delivering a maximum hydrogen generation of 2820 μmol g^{-1} h^{-1}, approximately ten times higher than that of bulk carbon nitride.

1 | Introduction

Conventional thermal polymerization for synthesizing carbon nitride exhibits limited crystallinity, textural properties, and poor control over bandgap engineering, which are essential for effective photocatalytic hydrogen production. Recently, carbon nitride derived from self-assembled complexes has demonstrated unique morphologies and high surface areas with excellent physical, chemical, and electronic properties. Also, supramolecular self-assembled precursor-derived carbon nitride (SSCN) is a versatile and environmentally benign material as hard- or soft-templates are not used in the synthetic process. The nitrogen-rich monomer units of carbon nitride precursors can self-assemble via weak intermolecular noncovalent interactions, such as van

der Waals forces, hydrogen bonding, electrostatic interactions, π–π stacking, and hydrophobic interactions. This molecular-level alignment of precursor molecules facilitates the synthesis of carbon nitride materials with exceptional textural properties. For instance, a self-assembled supramolecular complex for synthesizing carbon nitride can be formed from a single monomer unit, such as melamine, using a hydrothermal method. In this process, melamine is partially hydrolyzed to form cyanuric acid, which then self-assembles into a complex crystal intermediate structure with a uniform morphology [1]. A similar self-assembled complex structure can be synthesized using multiple precursors via noncovalent interactions [2].

Heteroatom doping in carbon nitride (phosphorous, sulfur, boron, oxygen, carbon, etc.) is a conventional strategy for modifying the band structure and reducing electron–hole recombination in photocatalytic materials [3]. A challenge in this area of study is the synthesis of carbon nitride (CN) with evenly distributed heteroatoms. This hurdle has been addressed by the self-assembly of monomer units that incorporate the targeted heteroatoms. For example, melamine can be self-assembled with trithiocyanuric acid to synthesize sulfur-doped carbon nitride, glucose/terephthalic acid/nicotinic acid to synthesize carbon-doped carbon nitride, oxalic acid/formic acid/urea to synthesize oxygen-doped carbon nitride, and phytic acid to synthesize phosphorus-doped carbon nitride [4–8]. In addition, supramolecular complex structures have been utilized to design new materials by developing metal single-atom-doped materials, metal oxide/phosphide heterostructures, and defect-engineered carbon nitride materials [9–12]. Melamine-based carbon nitride usually shows high thermal and chemical stability as well as spontaneous self-assembly with several other monomers. However, it is worth noting that other types of nitrogen-rich organic compounds can self-assemble to form intricate structures in different solutions. Nevertheless, most supramolecular-based carbon nitrides are unstable at high temperatures ($T > 500^\circ C$) and show less crystallinity, limiting their use as photocatalysts.

In contrast, the molten-salt-assisted method provides a liquid reaction medium for uniform polymerization and structural control of polymerized carbon nitride [13]. The carbon nitride synthesized via this method showed highly crystalline carbon nitrides with poly (heptazine imide) (PHI) and poly (triazine imide) (PTI) structures [14]. Several metal halogens (NaCl, KCl, LiCl, LiBr, KBr, etc) have been explored for the synthesis of crystalline carbon nitrites, which can be categorized into Na-PHI, K-PHI, K-Li PHI/PTI, and Li-PTI [15–18]. Furthermore, Na-PHI and K-PHI tend to form crystalline structures only at a high temperature of 600°C and 550°C, respectively [19]. This limits the ability to convert most supramolecular complex structures to SSCN because of their poor stability at higher temperatures. Regardless, LiCl or a eutectic mixture of LiCl, such as LiCl/KCl, with a low melting point has been used to synthesize highly crystalline carbon nitride at lower calcination temperatures. Because Li salts tend to direct carbon nitride toward the formation of triazine structures, a mixture of PTI/PHI structures is usually synthesized from the carbon nitride precursors in LiCl/KCl eutectic mixtures [20]. Hence, the synthesis of SSCN with a pure PHI structure is a major challenge. Nevertheless, recent reports have shown the possibility of overall water splitting using PTI and PHI/PTI heterostructures [21, 22]. Unfortunately, most reports employed full-arc irradiation ($\lambda > 325$ nm), hence limiting their practical application. For most photocatalytic applications, the carbon nitride with the PHI structure is superior to that with the PTI structure. However, the synthesis of SSCN-based crystalline carbon nitride with a pure PHI structure at low calcination temperature is still challenging [23].

In this study, we developed a novel supramolecular complex comprising cyanuric acid (CA) and nitrogen-rich 3-amino-1,2,4 triazole (AT) using a simple precipitation method. Herein, the CA monomer with a six-membered ring forms a noncovalent interaction with the 5-membered ring of AT to form a uniform sheet-like morphology. The morphology, stoichiometry, and physical, chemical, and optical properties of the material were altered by controlling the CA-to-AT monomer ratio during reorganization. While the general crystalline carbon nitride synthesized via a eutectic mixture of KCl/LiCl offers a mixture of PTI and PHI crystal structures, SSCN shows a highly crystalline sheet-like structure with a pure PHI structure owing to the prior confinement of monomers in a lamellar structure. SSCN with a PHI structure showed significantly enhanced photocatalytic performance for water splitting compared to bulk graphitic carbon nitride and the crystalline carbon nitrides with the mixture of PTI and PHI structure. X-ray diffraction (XRD), Fourier transform infrared spectroscopy (FTIR), X-ray photoelectron spectroscopy (XPS), and near-edge X-ray absorption fine structure spectroscopy (NEXAFS) were employed to investigate the structural properties of the catalyst, whereas UV–vis spectroscopy, photoluminescence spectroscopy (PL), time-resolved photoluminescence spectroscopy (TRPL), and ultraviolet photoelectron spectroscopy (UPS) were used to elucidate its band structure and optical properties. Additionally, theoretical calculations were used to examine the impact of Li and K incorporation on the electronic band structures of PHI and PTI carbon nitrides to support the experimental data.

2 | Results and Discussions

A schematic representation of the synthetic process for SSCN is shown in Figure 1a. The monomers dissolved in DMSO (AT and CA) were precipitated using ethanol to synthesize a supramolecular complex structure. The complex precursors were subjected to thermal polymerization using a molten-salt-assisted method (LiCl/KCl). The excess salt was removed by washing with HCl (2.0 M) and hot water. The morphological features of the self-assembled supramolecular complexes were analyzed using FESEM. Figure 1b–d demonstrates the different morphologies of complex formation at different molar ratios. This morphological transformation can be attributed to changes in the hydrogen-bonding environment between CA and AT, which serve as precursor monomers. CAT21-P, CAT22-P, and CAT23-P are the abbreviations given to supramolecularly synthesized carbon nitride precursors with CA to AT ratios of 2:1, 2:2, and 2:3, respectively. CAT21-P exhibited a cluster of small sheet-like structures (Figure 1b), but with an increase in the AT content (CAT22-P) led to well-defined large sheet-like structures (Figure 1c) within the micrometer range. This indicates a strong intermolecular hydrogen bonding interaction between CA and the AT monomers, restricted to a 2D plane. Also, a further increase in AT (CAT23-P) led to the formation of a 3D stacked

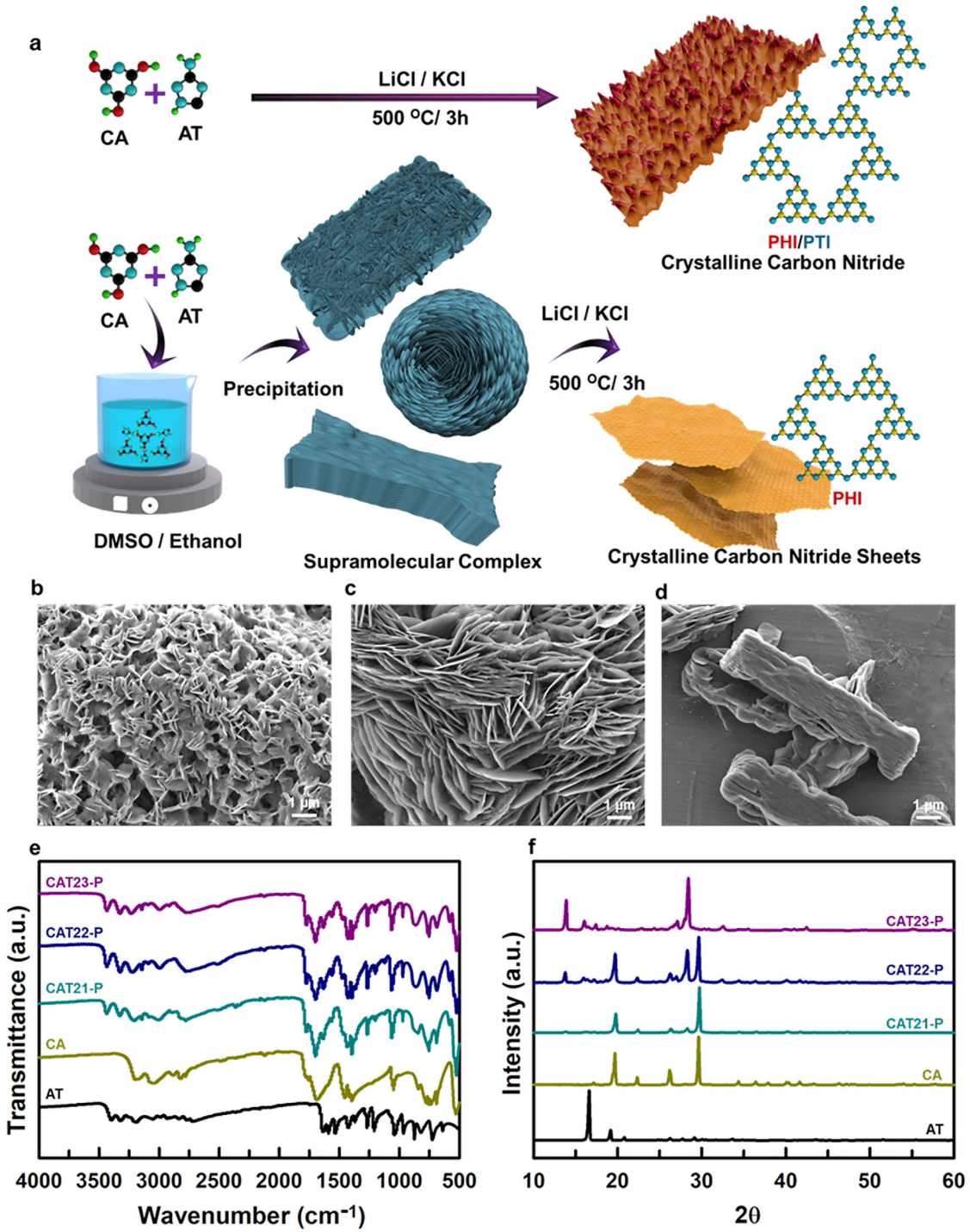

FIGURE 1 | a) Schematic illustration of the synthesis process of SSCN with PHI structure. FESEM images of supramolecular complexes prepared with different ratios of AT and CA (b) CAT21-P, (c) CAT22-P, and (d) CAT23-P. (e) FTIR spectra and (f) XRD patterns of AT, CA, CAT21-P, CAT22-P, and CAT23-P.

layered structure (Figure 1d), which may be due to the increased intramolecular hydrogen bonding interactions between the AT monomers. The FTIR spectra of the supramolecular complexes were compared with those of CA and AT, and the results are shown in Figure 1e. The peak at 1058 cm^{-1} of CA, corresponding to C—OH stretching vibrations, slightly shifted to a higher energy (1066 cm^{-1}) in the supramolecular complex, which is attributed to strong hydrogen bonding interactions between AT and CA [24]. A stronger peak around 1730–1770 cm^{-1} corresponding to C═O stretching vibrations is observed in the supramolecular complex. This can be attributed to the formation of tautomeric isomers of CA [25]. Additionally, the peak at 3402 cm^{-1} corresponding to the N-H_2 symmetric stretching vibrations in AT blueshifted to 3436 cm^{-1} in supramolecular precursors due to the formation of hydrogen bonding [26]. According to the XRD analysis (Figure 1f), all the self-assembled materials demonstrated the disappearance

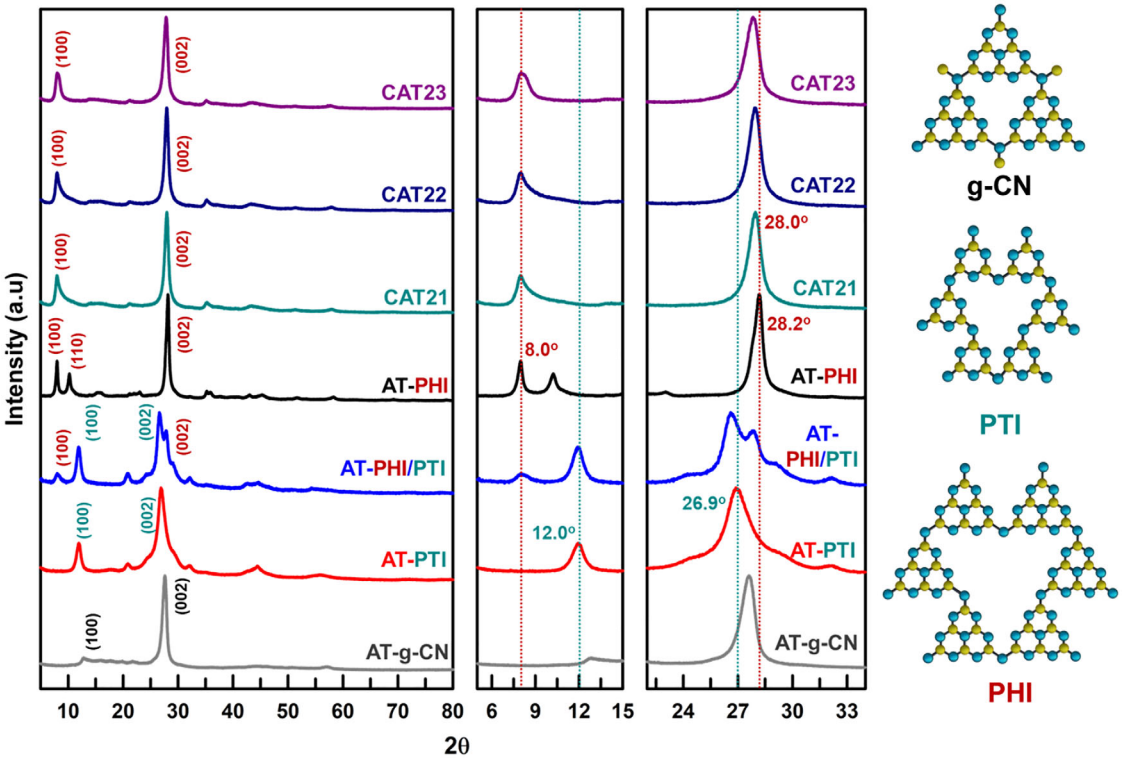

FIGURE 2 | XRD patterns of CAT21, CAT22, CAT23, AT-PHI, AT-PHI/PTI, AT-PTI, AT-g-CN, and the crystal structures of g-CN, PTI, and PHI.

of peaks corresponding to AT, indicating the formation of a supramolecular complex between AT and CA. The XRD patterns of CAT21-P and CAT22-P revealed new supramolecular complexes mixed with trace amounts of CA, while CAT23-P exhibited completely new XRD patterns that were different from those of CA and AT, suggesting the formation of a novel self-assembled structure.

The prepared supramolecular self-assembled complexes were used for synthesizing crystalline carbon nitride via thermal polymerization using a molten-salt-assisted method [27]. An optimized eutectic mixture of LiCl (20 mmol) and KCl (60 mmol) at 500°C in a nitrogen atmosphere was used as the medium to introduce defects while preserving the crystallinity of the polymerized carbon nitride. The synthesized SSCN from the precursor complex of CAT21-P, CAT22-P, and CAT23-P was named as CAT-21, CAT22, and CAT23, respectively. For reference, various crystalline carbon nitrides were synthesized from AT, as a precursor, in the different molten salt conditions, such as KCl, LiCl, and the KCL/LiCl eutectic mixture, which were named as AT-PHI, AT-PTI, and AT-PHI/PTI, respectively (Table S1).

The crystal structures of the SSCN were characterized by powder XRD analysis. The SSCN prepared through the molten salt-assisted approach exhibited multiple sharp peaks and a completely different XRD pattern compared to that of the bulk g-CN, indicating the formation of highly crystalline carbon nitride (Figure 2). The peaks corresponding to the (002) and (100) planes of g-CN at 27.2° and 12.9° completely disappeared, and distinct sharp peaks at 28.0° (002) and 8.0° (100) emerged prominently, indicating the formation of PHI structure. A gradual transformation from g-CN (at 450°C) to PHI structure (at 475°C–525°C) was observed by varying the thermal polymerization temperature from 450°C to 525°C as displayed in Figure S1a. At high temperatures (>525°C), the supramolecular complex-derived carbon nitride completely disintegrated. It is worth noting that no peaks corresponding to the PTI structure were observed in the series of supramolecular complex-derived carbon nitride. As a reference, we prepared carbon nitride with different crystalline structures from AT under different alkaline salt conditions. Thermal polymerization of AT in LiCl at 500°C generates carbon nitride with a PTI structure (AT-PTI), whereas AT in KCl at 550°C produces carbon nitride with a PHI structure (AT-PHI). However, the thermal treatment of AT in a eutectic mixture of KCl and LiCl at 500°C induced carbon nitride with a mixed crystal structure of PHI and PTI (AT-PTI/PHI). The polymerization in LiCl at 500°C favors PTI formation due to Li^+ stabilization of triazine units, whereas KCl at 550°C promotes PHI formation by stabilizing heptazine units (Figure 2). The eutectic mixture of LiCl and KCl reduces the melting point, enabling the simultaneous nucleation of both phases, resulting in PHI/PTI heterostructure (Table S1). The molten salt medium enhances the solubility of precursors and intermediates, facilitating uniform nucleation and prompting long-range ordered crystal growth of PHI and PTI carbon nitrides. Since Li^+ has the tendency to depolymerize the heptazine-based monomers to triazine-based monomers and stabilize them during the cooling, it is important to increase the KCl to LiCl ratio to get more PHI structure rather than that of PTI structure and achieve a maximum photocatalytic hydrogen evolution (Figure S2 and Table S1) [28]. However, if the LiCl content is too low or if only KCl is used (AT-1, Figure S2), the carbon nitride tends to form a conventional g-CN structure at 500°C, rather than a crystalline PTI/PHI structure. Hence, pure PHI structure at relatively low temperature (~500°C) is not

possible by conventional methods. This result is different from that of the carbon nitride synthesized under the same conditions using CAT21, CAT22, and CAT23, where carbon nitride with only PHI structure was obtained without PTI impurities. This suggests that the orientation of the supramolecular complex precursor plays an important role in directing the formation of a single-phase PHI crystal structure in carbon nitride.

It is worth noting that the thermal polymerization of AT, CA, and a physical mixture of AT and CA using the molten salt-assisted method (LiCl/KCl eutectic mixture at 500°C) also produced carbon nitride with a mixed PHI/PTI phase (Figure 2; Figure S1b). Most importantly, the (002) peak corresponding to the interlayer distance of synthesized carbon nitrides significantly changed depending on the crystal structure. The interlayer distances of PHI, g-CN, and PTI carbon nitrides are typically 3.16 Å ($2\theta = 28.2°$), 3.23 Å ($2\theta = 27.6°$), and 3.30 Å ($2\theta = 26.9°$), respectively, as displayed in Figure 2. The CAT21, CAT22, and CAT23 samples also exhibited a peak around 28.0° without a shoulder peak at 26.9°, indicating a complete transformation to the PHI structure. Also, the d-spacing calculated from the (100) peak, representing the in-plane periodicity of the triazine or heptazine units in the crystalline carbon nitride for the PHI, g-CN, and PTI structure was calculated to be ~10.99 Å ($2\theta = 8.0°$), ~6.83 Å ($2\theta = 12.9°$), and ~7.4 Å ($2\theta = 12.0°$), respectively [29]. The (100) peak position of the CAT21, CAT22, and CAT23 samples was observed at 8.0°, which is the same as that of the carbon nitride with the PHI structure. Also, in supramolecular complex-derived carbon nitrides, an increase in AT content within the precursor complex led to broadening of the (100) peak, suggesting reduced crystallinity in the ab plane direction of the PHI structure.

The carbon nitride structure and functional groups were further analyzed by attenuated total reflectance-Fourier transform infrared (ATR-FTIR) spectroscopy (Figure S3). All samples exhibited a broad peak around 3000–3200 cm^{-1}, which can be attributed to the stretching vibrations of the terminal —NH_2 and —NH— functional groups. The peak around 3300 cm^{-1} was ascribed to the hydroxyl stretching vibrations of the adsorbed water molecules. The characteristic peaks of the bending and stretching modes of N—C═N in the triazine or heptazine units were observed at 795 cm^{-1} and 1250–1600 cm^{-1}, respectively. Notably, the crystalline carbon nitride obtained from the salt-assisted method (PHI, PTI) exhibited a peak at 2170 cm^{-1}, corresponding to the asymmetric stretching modes of the unpolymerized terminal cyano group [30].

High-resolution transmission electron microscopy (HRTEM) images showed a few layers of stacked lamellar crystalline CN sheets (Figure 3a–d) with clear lattice fringes and grain boundaries. Lattice fringes with d spacings of ~1.1 nm were observed in the CAT21, CAT22, and CAT23 samples (Figure 3a–c), corresponding to the (100) plane of the PHI structure, which is in good agreement with the XRD analysis. In contrast, the AT-PTI sample exhibited lattice fringes with a d-spacing of ~0.75 nm, corresponding to the (100) plane of the PTI structure (Figure 3d). It was also noted that the specific surface area of all the SSCN samples was much higher than that of the bulk carbon nitrides. CAT21, CAT22, and CAT23 showed BET surface areas (Figure S4a) of 85.7, 108.2, and 50.4 m^2/g, respectively, while AT-PHI, AT-PTI, AT-PHI/PTI, and AT-g-CN (Figure S4b) had lower surface areas of 7.1, 6.2, 19.4, and 6.2 m^2/g, respectively.

Near-edge X-ray absorption fine structure (NEXAFS) and X-ray photoelectron spectroscopy (XPS) studies were conducted to determine the local electronic configurations and chemical structures of SSCN. The C K-edge spectra (Figure S5a) showed a low-intensity peak corresponding to the 1s→ $\pi^*_{C=C}$ transition at 285.1 eV and two high-intensity peaks corresponding to 1s→ $\pi^*_{N=C-N}$ at 287.9 and 288.5 eV. The broad peak at approximately 287 eV and the small shoulder peak at 287.2 eV could be assigned to the 1s → σ^* transitions of C—N and C—H, respectively. The nitrogen K-edge NEXAFS spectra (Figure S5b) displayed three characteristic resonances of 1s→ π^* transitions corresponding to C—N═C, graphitic N—$(C)_3$, and N—$(C)_3$ bridging at 399.4, 401.2, and 402.4 eV, respectively.

The XPS survey spectra confirmed the presence of C, N, and O, whereas only trace amounts of Li and K ions were detected (Figure S6). This indicates the effective removal of alkali metal ions after washing with hot water and a 2.0 M HCl. The deconvoluted XPS C1s spectra (Figure 4a) revealed three major peaks at approximately 284.7, 286.2, and 288.3 eV, corresponding to sp^2 hybridized graphitic carbon atoms (C═C), carbon attached to terminal amino groups (C—NH_x), and sp^2 hybridized N—C═N carbon within the ring structure (triazine and tris-s-triazine), respectively. The AT-PHI structure exhibited a slightly higher binding energy (288.5 eV), corresponding to the N—C═N carbon species, than the AT-PTI structure (288.0 eV) due to the more conjugated connections in the tris-s-triazine unit. The binding energies of the N—C═N carbon species in the CAT21, CAT22, and CAT23 samples were 288.3, 288.4, and 288.3 eV, respectively, which are closer to the PHI structure. The reference AT-PHI/PTI sample with a PTI-PHI mixed crystal structure (as indicated by XRD) showed a binding energy of 288.0 eV, which is close to that of the pure AT-PTI sample. The deconvoluted N 1s XPS spectra (Figure 4b) exhibit three major peaks that can be assigned to sp^2 hybridized N—C═N species, terminal amino groups (C—NH_x), graphitic/bridging nitrogen species (N—C_3/ C—NH—C). The AT-PHI and AT-PTI structures show peaks corresponding to the N—C═N bond at binding energies of 398.9 and 398.7 eV, respectively. This slight shift in energy can be attributed to the difference in the conjugated ring structure between tris-s-triazine and triazine. In the PHI structure, a peak corresponding to the C—NH—C and N—C_3 is located at 400.7 eV, whereas the AT-PTI exhibited a peak at 400.1 eV, corresponding solely to C—NH—C, consistent with the absence of graphitic nitrogen in the PTI structure [31, 32]. The AT-PTI/PHI sample exhibited a binding energy similar to that of the PTI structure. In contrast, the supramolecular complex-derived CAT21, CAT22, and CAT23 samples displayed higher binding energies for C—NH—C/N—C_3 than the C—NH—C of the AT-PTI structure, indicating the formation of the PHI structure [29]. The relative peak areas of all the samples are tabulated in Table S2. To confirm the change in the binding energy associated with the structural differences between the PTI and PHI carbon nitrides, we analyzed the PTI and PHI carbon nitrides derived from dicyandiamide (DCDA), as illustrated in Figure S7. The PHI carbon nitride derived from AT and DCDA showed similar binding energies. In contrast, the PTI carbon nitride derived from DCDA exhibited a slight shift toward a

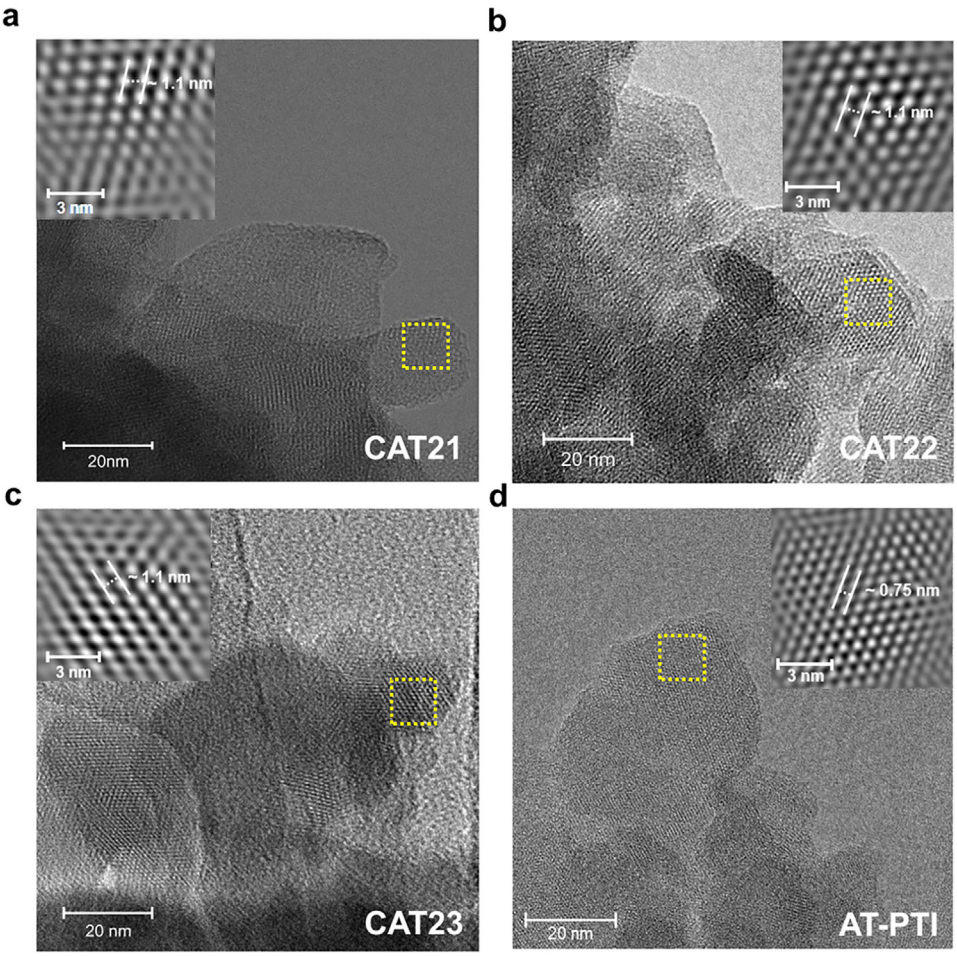

FIGURE 3 | TEM images of (a) CAT21, (b) CAT22, (c) CAT23, and (d) AT-PHI.

higher binding energy compared to AT-PTI, while still following the overall trend.

The photocatalytic performance largely depends on the optical characteristics and band structure of the photocatalyst. Most reported PHI and PTI structures exhibit a bandgap in the range of 2.00 to 3.00 eV, which is ideal for different photocatalysis applications [10, 33, 34]. The bandgap of the photocatalyst determines the light absorption capability and utilization of visible light. According to UV–vis diffuse reflectance spectroscopy analysis (UV–vis DRS), CAT21 and CAT22 showed similar absorption behavior, whereas the CAT23 sample with high AT content exhibited a significant redshift due to the high nitrogen content (Figure 5a). The indirect bandgap was determined using a tauc plot of the Kubelka–Munk value [35], where the CAT21, CAT22, CAT23, AT-PTI, AT-PHI, and AT-PHI/PTI exhibited bandgap of 2.78, 2.79, 2.51, 2.1, 2.76, and 2.7 eV, respectively (Figure 5b; Figure S8b). AT-PTI (2.1 eV) had a narrower band gap compared to AT-PHI (2.76 eV) and AT-PTI/PHI (2.7 eV). In carbon nitride structures, the valence band (VB) is primarily derived from N 2p lone pair electrons of the electron-rich nitrogen atoms, while the conduction band (CB) is mainly formed by antibonding π^* orbitals associated with C 2p states of electron-deficient carbon atoms [36]. Additionally, structural defects like vacancies, doping, and functionalization can generate intermediate energy states within the bandgap. Moreover, the presence of alkali metal ions within the carbon nitride framework can significantly influence the bandgap, a phenomenon we have investigated through theoretical calculation in the following sections. All the carbon nitride samples were thoroughly washed with 2.0 M HCl and hot water to remove alkali metal ions; however, trace amounts of Li and K were still detected by XPS analysis (<1%). The narrow bandgap of AT-PTI is due to the high nitrogen content and intercalated Li and K ions. The band alignment of the photocatalyst was determined using UPS analysis (Figure 5c; Figure S9) [37]. The Fermi level of the catalyst was extracted from the work function (φ) determined from the UPS spectra (Table S3). The valence band minimum (VBM) positions were determined by extrapolating the valence band edge, as shown in Figure 5d. The position of the conduction band minimum (E_{CBM}) was determined using the equation $E_{CB} = E_g - E_{VB}$, and the corresponding band diagram is illustrated in Figure 5e. CAT21 exhibited more negative E_{CBM} (−0.30 eV) than CAT22 (−0.26 eV) and CAT23 (−0.23 eV). While the E_{CBM} of AT-PTI (−0.19 eV) was closer to the redox potential of hydrogen, AT-PHI showed a more negative E_{CBM} (−0.78 eV) compared to all other samples, indicating a stronger reduction potential of its photoelectrons.

Modifying the structure and crystallinity of carbon nitride can influence not only its electronic characteristics but also its electron–hole recombination rate and charge transfer efficiency. When a photocatalyst is excited with photons with energies

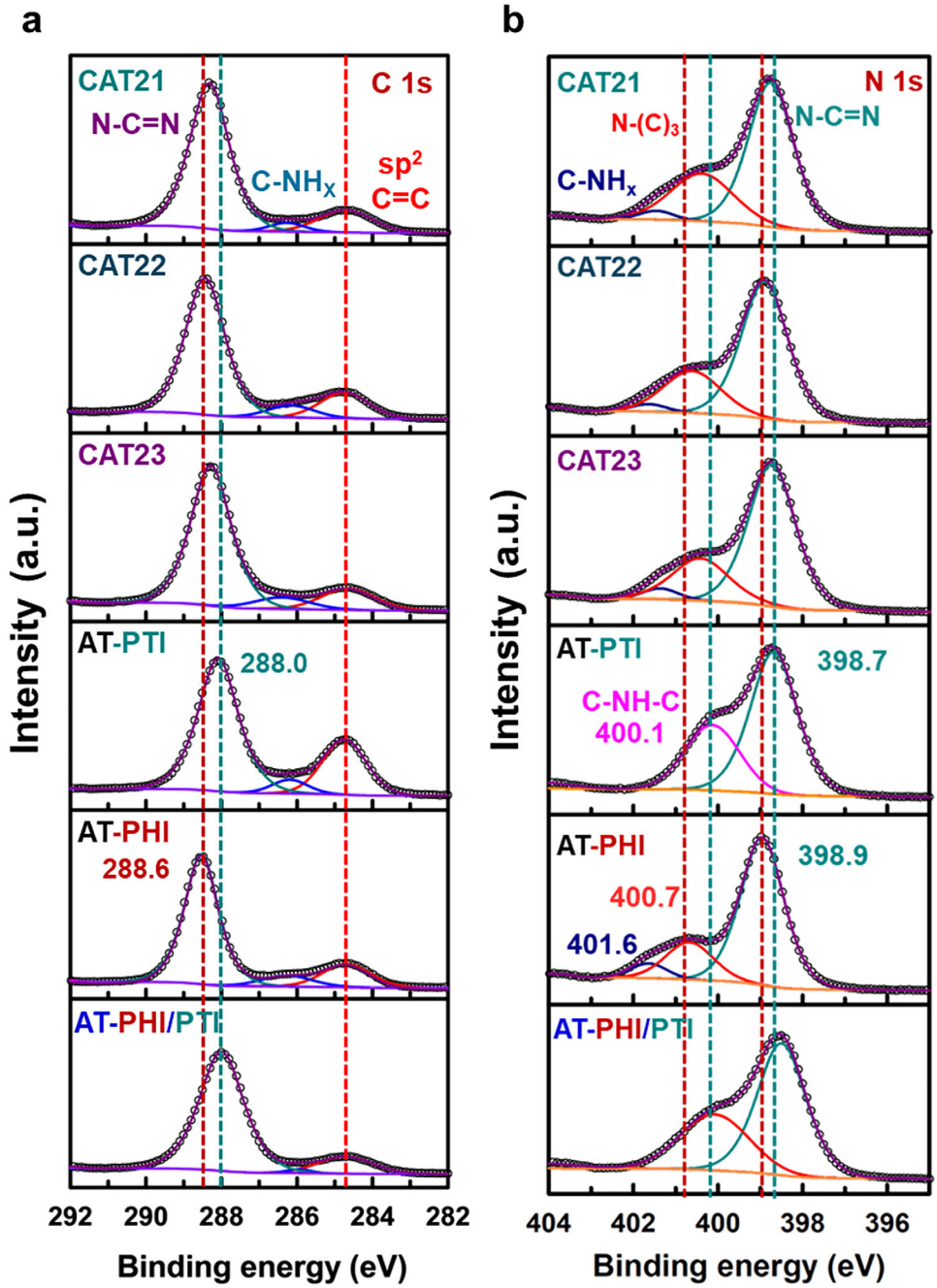

FIGURE 4 | XPS a) C 1s and b) N 1s spectra of CAT21, CAT22, CAT23, AT-PHI, AT-PTI, and AT-PHI/PTI.

higher than its bandgap ($h\nu > E_g$), electron–hole pairs are generated and separated. However, these photogenerated electrons tend to quickly recombine with holes, leading to the emission of light (fluorescence) through radiative electron–hole recombination. The recombination characteristics of the photoinduced charge carriers were evaluated using photoluminescence (PL) spectroscopy. The PL intensity is directly proportional to the emitted photons upon electron–hole recombination, and the lower intensity of the fluorescence spectra indicates a retarded electron–hole recombination process in the photocatalyst. Here, AT-g-CN showed the highest PL intensity, followed by AT-PTI, AT-PHI, AT-PHI/PTI, CAT21, CAT22, and CAT23 (Figure 6a). On the other hand, the AT-PTI exhibited PL peaks at approximately 430 and 480 nm, similar to those observed for AT-PHI/PTI. In contrast, the AT-PHI structure displayed strong emissions near 500 nm, resembling the emissions seen in CAT31, CAT22, and CAT23. This observation further suggests that SSCN predominantly exhibits a PHI structure rather than a PTI structure. The steady-state PL spectra provide insights into the radiative recombination of photogenerated electron–hole pairs in carbon nitride with different crystal structures. However, to understand the non-radiative relaxation, possibilities of trapped states, and separation of charge carriers before recombination, we performed time-resolved photoluminescence (TRPL) spectroscopy. The radiative lifetimes of the different samples are tabulated in Table 1. The TRPL decay of the PHI carbon nitrides was much longer than that of the PTI containing carbon nitrides (Figure 6b). The PHI samples, AT-PHI, CAT21, CAT22, and CAT23, exhibited average

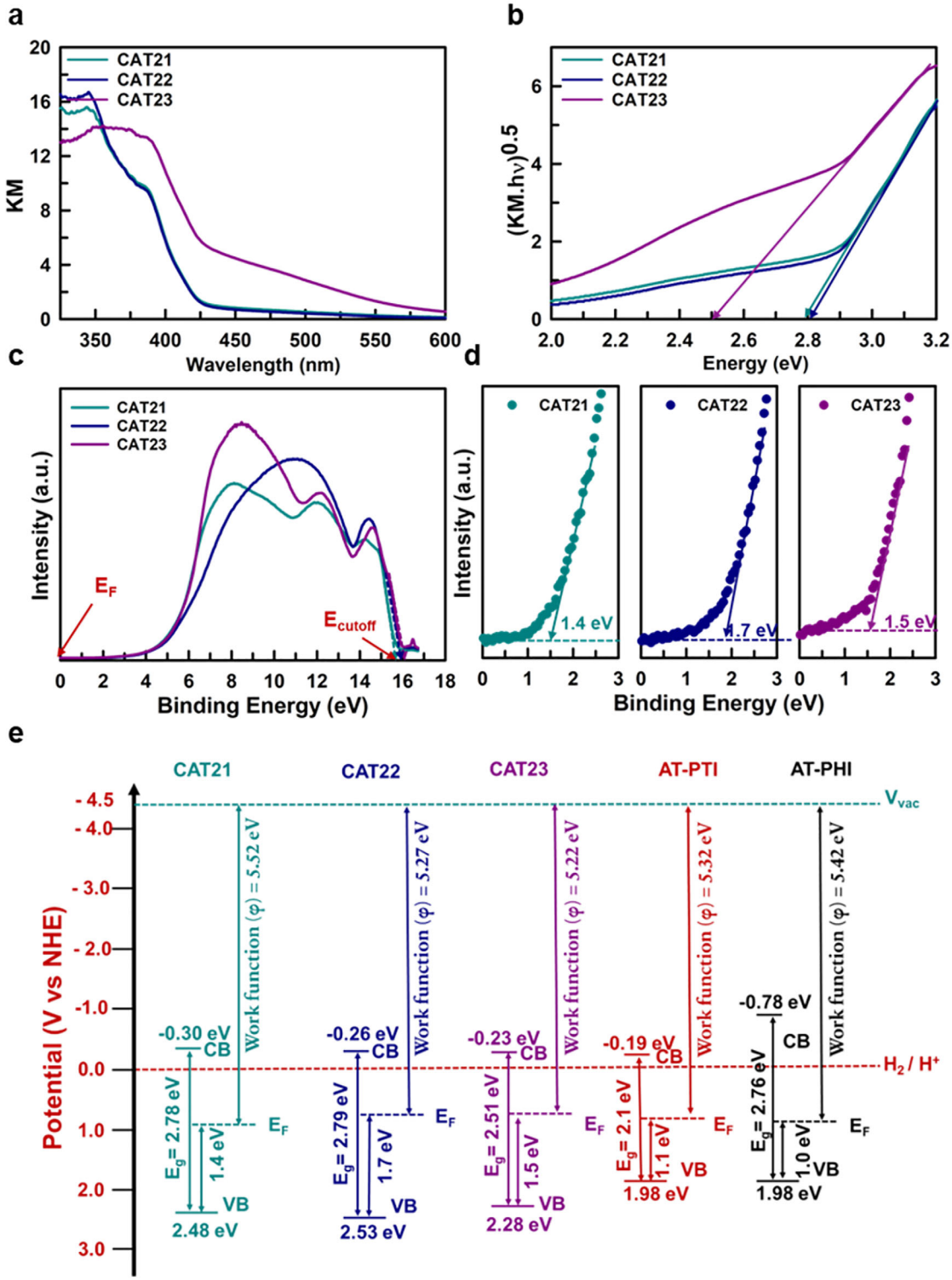

FIGURE 5 | (a) UV–vis DRS spectra, (b) Tauc plot, (c) UPS spectra, and d) UPS valence band region of CAT21, CAT22, and CAT23 samples. (e) Illustration of bandgap alignment (V vs. NHE) of CAT21, CAT22, CAT23, AT-PHI, AT-PTI, and AT-PHI/PTI samples.

lifetimes (τ_{avg}) of 7.03, 2.32, 2.52, and 1.88 ns, respectively. In contrast, the AT-PHI/PTI and AT-PTI samples showed much shorter τ_{avg} values of 1.28 and 0.86 nm, respectively.

Generally, most defects in carbon nitrides are paramagnetic in nature and can be detected using electron paramagnetic resonance (EPR) spectroscopy. The concentration of defect centers/unpaired electrons in different carbon nitride samples was analyzed using EPR spectra. As shown in Figure 6c, the Lorentzian line (g = 2.005) of the AT-PTI sample showed the highest defect concentration, followed by AT-PTI/PHI, CAT23, CAT22, CAT23, and AT-PHI. Compared to the PHI structure, the PTI structure exhibited a significantly higher number of unpaired electrons, due to the increased defect concentration, terminal

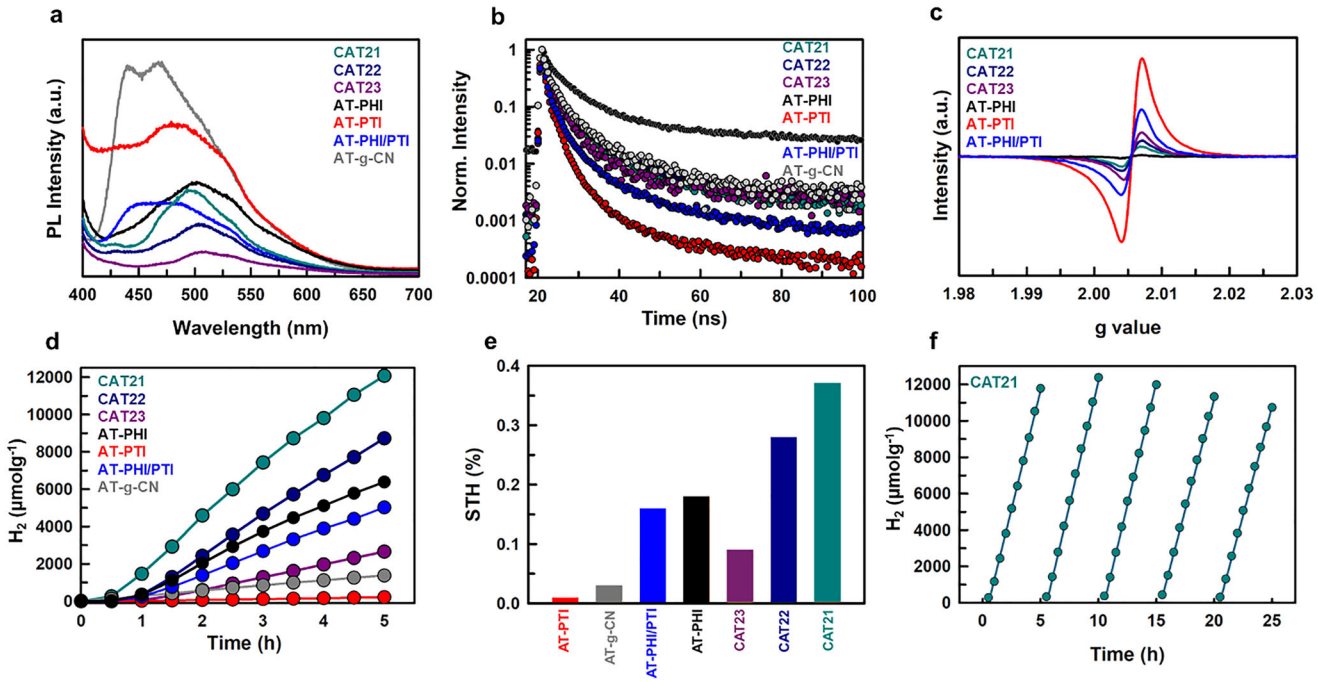

FIGURE 6 | (a) Steady-state PL spectra, (b) time-resolved transient PL spectra, (c) EPR spectra, (d) photocatalytic hydrogen generation measurements, and (e) Solar-to-Hydrogen percentage of different photocatalysts. (f) The long-term photocatalytic stability test of CAT21 for 25 h.

TABLE 1 | Radiative lifetimes from fitted decay spectra of CAT21, CAT22, CAT23, AT-PHI, AT-PTI, and AT-PHI/PTI.

Sample	τ_1 (ns)	τ_2 (ns)	τ_3 (ns)	τ_{avg} (ns)
AT-PHI	1.89	8.32	121.60	7.03
CAT21	1.03	5.56	49.28	2.32
CAT22	0.93	6.02	71.22	2.52
CAT23	0.76	3.83	65.27	1.88
AT-PHI/PTI	0.65	3.56	32.58	1.28
AT-PTI	0.48	2.38	17.34	0.86

groups, and incomplete condensation sites. These defects can act as photogenerated electron–hole recombination centers, which can drastically reduce the photocatalytic efficiency of the material [28]. The defect concentration in CAT21< CAT22< CAT23< AT-PHI/PTI< AT-PTI, which directly reflects its photocatalytic activity. The photocatalytic performance of SSCN materials was determined using a top-illuminated reactor under a solar simulator equipped with a 1.5 G air-mass filter (0.1 Wcm^{-2}). Here, the Pt cocatalyst was in situ photodeposited, and triethanolamine (TEA) was used as a hole scavenger. Under these conditions, while the photogenerated holes are consumed by TEA, the photoinduced electrons migrate to the Pt cocatalyst sites to reduce the protons in water, leading to the generation of hydrogen gas. The evolved hydrogen was periodically quantified using an online GC. The carbon nitride samples exhibited less hydrogen generation in the initial 30 min, which could be attributed to the photodeposition process of Pt on the photocatalyst. All SSCN materials showed excellent photocatalytic activity compared to bulk g-CN. The CAT21 carbon nitride sample exhibited the highest hydrogen generation rate of 2819 μmol $h^{-1}g^{-1}$, which was ten times higher than that of bulk g-CN (281 μmol $h^{-1}g^{-1}$). In comparison, CAT22 and CAT23 exhibited photocatalytic hydrogen generation rates of 2168 and 646 μmol h^{-1} g^{-1} of hydrogen, respectively (Figure 6d). The bandgaps CAT21 and CAT22 are very close, yet the photocatalytic performance of CAT21 was relatively better, which can be attributed to its low surface defects (EPR) and relatively higher reduction potential at the CB edge (−0.30 eV) compared to CAT22 (−0.26 eV), which is evident from the UPS spectra. While CAT23 demonstrated a low charge recombination rate and long-range visible light absorption property, the lower conduction band edge (−0.23 eV) might hinder efficient hydrogen production on the surface-active sites. We also tested CAT21 samples prepared at different temperatures to understand their dependence on the photocatalytic performance (Figure S10). It is worth noting that the sample prepared at 525°C performed very close to that of the 500°C sample, but the amount of product obtained after thermal polymerization was three times lower than that of the latter. Also, increasing the calcination temperature to 550°C did not yield any products. This may be due to the thin sheet-like morphology of the supramolecular complex, which is relatively unstable at higher temperatures. Moreover, the AT-PHI structure provided the best hydrogen production of 1624 μmol h^{-1} g^{-1} among the AT-derived carbon nitride samples, followed by AT-PHI/PTI (904 μmol h^{-1} g^{-1}), AT-g-CN (281 μmol h^{-1} g^{-1}), and AT-PTI (48 μmol h^{-1} g^{-1}). The solar-to-hydrogen (STH) conversion efficiency of the catalyst under AM 1.5 irradiation is calculated using Equation S1 and shown in Figure 6e (Table S1). The STH conversion efficiency of CAT21 is 0.37%, which is comparable to the other reports in this field (Table S4). The stability of the photocatalyst was evaluated for five consecutive cycles for a total reaction time of 25 h (Figure 6f) without replenishing the hole-scavenger. The supramolecularly derived

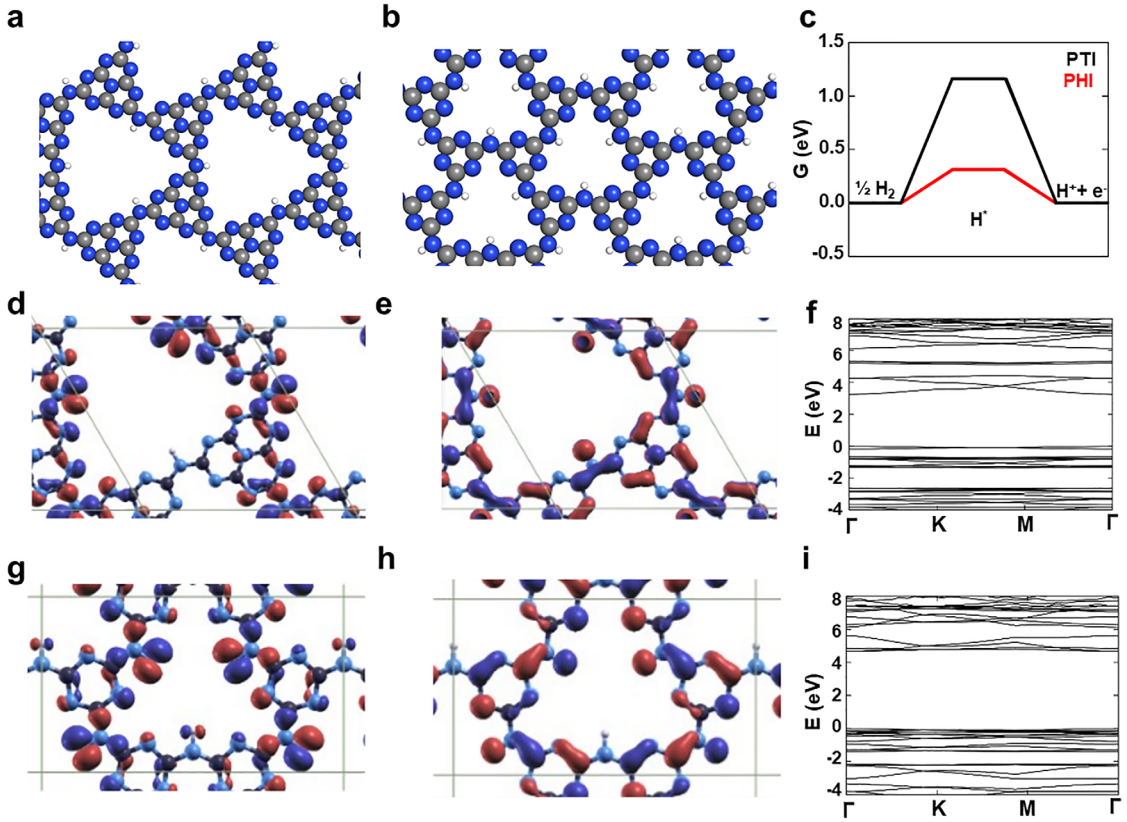

FIGURE 7 | Representative model structures of carbon nitrides with a) PHI and b) PTI used in quantum chemical calculations. Color code: blue–N, gray–C, and white–H. c) Reaction free energy diagram for HER on pristine PHI and PTI. HOMO, LUMO, and band structure for pristine (d–f) PHI and (g–i) PTI, respectively.

carbon nitride with a PHI structure (CAT21) exhibits stable hydrogen generation without significant performance decay. The slight reduction in activity can be attributed to the gradual consumption of LA during the photocatalysis reaction, with the H_2 evolution decreasing from 11783 μmol·g^{-1} in the first cycle to 10737 μmol·g^{-1} in the fifth cycle. After the stability test, the photocatalyst was recovered and characterized using XRD, FTIR, and HR-TEM. As shown in Figure S11, no significant changes were observed in the XRD patterns and FTIR spectra before and after the photocatalytic reaction, indicating excellent structural and chemical stability of the developed CAT21 carbon nitride sample. HR-TEM analysis further confirmed that the photocatalyst retained its crystal structure even after 25 h of continuous operation (Figure S12a,c). In addition, EDX elemental mapping showed uniform Pt photodeposition on the catalyst surface when both LA and TEA were used as hole scavengers. (Figure S12b,d).

3 | Computational Insights

To better understand the photocatalytic performance of SSCN with different structures (PHI and PTI, as displayed in Figure 7a,b), we conducted theoretical calculations for the hydrogen production behavior. Since the XPS results show non-negligible amounts of metal ions (K and Li), we also studied the doped versions of PHI and PTI with K, Li, and the counter-ion Cl, as shown in Figure S13.

First, the Gibbs free energy for the adsorption of active hydrogen H* was calculated to estimate the photocatalytic performance for producing hydrogen, which should ideally be around zero for efficient performance. As shown in Figure 7c, the Gibbs free energy of PHI carbon nitride was 0.38 eV, which was significantly lower than that of PTI carbon nitride (1.17 eV). This result suggests that the PHI structure can produce hydrogen more efficiently than PTI carbon nitride, which is in good agreement with the photocatalytic HER experimental results, as shown in Figure 6d. Furthermore, intercalated Li and K change this value considerably and non-monotonously, showing that an optimum (not too high and not too low) concentration of metal ions is beneficial (Table S5).

We also analyzed the band gaps, CBM, and VBM using a hybrid HSE06 functional (Table S5) [38]. The carbon nitride with the PHI structure exhibited a bandgap of 3.26 eV, which is close to the experimentally evaluated bandgap using UV–vis spectroscopy, while PTI carbon nitride showed a much higher bandgap (4.69 eV). These values differ from the experimental values because (i) real samples are more complex and not simple structures, often consisting of mixtures or containing point defects, and (ii) even hybrid DFT calculations introduce some error when describing electronic properties. Additionally, the presence of metal ions can further decrease the bandgap (Table S5). Finally, the HOMO, LUMO, and band structures of pristine PHI and PTI are shown in Figure 7d–i, which explains their fundamentally different activities and electronic structures.

In PHI, the LUMO orbital extends over the nitrogen and hydrogen atoms in the structure, which is crucial for photocatalytic HER activity. However, the LOM orbitals of PTI do not overlap with the nitrogen and hydrogen atoms, indicating the inertness of hydrogen, leading to a low photocatalytic HER performance. From the above calculations, it is evident that PHI carbon nitride is more suitable for hydrogen production than PTI carbon nitride. This has been experimentally confirmed as the PHI structures, such as AT-PHI, CAT21, CAT22, and CAT23, outperforming quite significantly than the pristine PTI structure, such as AT-PTI, in the photocatalysis of water.

4 | Conclusion

In summary, the low crystallinity and limited stability of supramolecular precursor complexes at high calcination temperatures limit their application in the synthesis of crystalline carbon nitride for photocatalytic applications. In this report, we demonstrate the synthesis of crystalline carbon nitride with an undesirable mixed crystal structure (PHI/PTI) by mixing aminotriazole and cyanamide, followed by treatment with an eutectic mixture of KCl and LiCl. We also demonstrated, for the first time, the possibility of converting a supramolecular-derived complex structure to a specific carbon nitride structure (e.g., PHI) using a eutectic mixture of KCl/LiCl, owing to the specific molecular orientation in a self-assembled structure. The carbon nitride structure was well characterized using XRD, FTIR, and XPS analysis to determine the exact crystal structure formation. The optical band structure of SSCN was further analyzed using UPS and UV–vis spectroscopy. The nature of electron–hole recombination was evaluated using steady-state PL spectra and time-resolved transient PL spectra. From the current study, it is evident that the PTI and PHI/PTI structures are not as active in hydrogen generation as the PHI structure. CAT21, CAT22, and CAT23 exhibited a pure PHI structure with significantly high photocatalytic activities. This might be due to the optimal CB edge position and the extended carrier lifetime in the PHI structure, which enhances its photocatalytic hydrogen generation efficiency. In conclusion, this study proposes the utilization of supramolecular complex molecules to derive specific carbon nitride structures, which will help further tune the performance of carbon nitride for various applications.

Acknowledgements

The authors acknowledge the Sydney Analytical Center at the University of Sydney and the Mark Wainwright Analytical Centre at the University of New South Wales for providing them with access to their facilities and technical support for this study. The authors also acknowledge the support of Dr. Christopher Bailey, Sydney Nanoscience Hub, The University of Sydney, for the TR-PL measurement.

Open access publishing facilitated by The University of Newcastle, as part of the Wiley - The University of Newcastle agreement via the Council of Australasian University Librarians.

Funding

This research was supported by a grant from the National Research Foundation of Korea and funded by the Ministry of Science, ICT, and Future Planning. (Grant No. 2022K1A4A8A01080312). We also acknowledge the support of NEXAFS analysis at the soft X-ray spectroscopy beamline of the Australian Synchrotron (Reference No: AS223/SXR/18955). Financial support from the Slovenian Research Agency is gratefully acknowledged through core funding P2-0152 (B. L.), project funding J7-4638 (B. L.) and N1-0303 (M. H.), and infrastructure funding I0-0039 (M. H.). The computational resources were funded through the HPC RIVR consortium and EuroHPC JU and provided by the HPC system Vega at the Institute of Information Science, Maribor, Slovenia.

Conflicts of Interest

The authors declare no competing interests.

Data Availability Statement

The datasets generated during and/or analyzed during the study are available from the authors on reasonable request.

References

1. S. Guo, Z. Deng, M. Li, et al., "Phosphorus-Doped Carbon Nitride Tubes With a Layered Micro-nanostructure for Enhanced Visible-Light Photocatalytic Hydrogen Evolution," *Angewandte Chemie International Edition* 55, no. 5 (2016): 1830–1834, https://doi.org/10.1002/anie.201508505.

2. Y.-S. Jun, E. Z. Lee, X. Wang, W. H. Hong, G. D. Stucky, and A. Thomas, "From Melamine-Cyanuric Acid Supramolecular Aggregates to Carbon Nitride Hollow Spheres," *Advanced Functional Materials* 23, no. 29 (2013): 3661–3667, https://doi.org/10.1002/adfm.201203732.

3. A. M. Sadanandan, M. Fawaz, N. P. Dharmarajan, et al., "Mesoporous C-Doped C_3N_5 as a Superior Photocatalyst for CO_2 Reduction," *Applied Catalysis B: Environment and Energy* 362 (2025): 124701.

4. T. Fei, C. Qin, Y. Zhang, et al., "A 3D Peony-Like Sulfur-Doped Carbon Nitride Synthesized By Self-Assembly For Efficient Photocatalytic Hydrogen Production," *International Journal of Hydrogen Energy* 46, no. 39 (2021): 20481–20491.

5. B. Zhao, J. Xu, Y. Liu, J. Fan, and H. Yu, "Amino Group-Rich Porous G-C_3N_4 Nanosheet Photocatalyst: Facile Oxalic Acid-induced Synthesis and Improved H_2-Evolution Activity," *Ceramics International* 47, no. 13 (2021): 18295–18303.

6. J. Wen, S. Zhang, Y. Liu, and Y. Zhai, "Formic Acid Assisted Fabrication of Oxygen-Doped Rod-Like Carbon Nitride with Improved Photocatalytic Hydrogen Evolution," *Journal of Colloid and Interface Science* 624 (2022): 338–347.

7. K. Liu, J. Ma, X. Yang, et al., "Phosphorus/Oxygen Co-Doping In Hollow-Tube-Shaped Carbon Nitride for Efficient Simultaneous Visible-Light-Driven Water Splitting and Biorefinery," *Chemical Engineering Journal* 437 (2022): 135232.

8. N. Panangattu Dharmarajan, M. Fawaz, C. Sathish, et al., "Insights into Atomic Level π-Electron Modulations in Supramolecular Carbon Nitride Nanoarchitectonics for Sustainable Green Hydrogen Production," *Advanced Energy Materials* 14, no. 29 (2024): 2400686.

9. X. Xiao, Y. Gao, L. Zhang, et al., "A Promoted Charge Separation/Transfer System from Cu Single Atoms and C_3N_4 Layers for Efficient Photocatalysis," *Advanced Materials* 32, no. 33 (2020): 2003082.

10. S. Liu, V. Diez-Cabanes, D. Fan, et al., "Tailoring Metal-Ion-Doped Carbon Nitrides for Photocatalytic Oxygen Evolution Reaction," *ACS Catalysis* 14, no. 4 (2024): 2562–2571.

11. N. P. Dharmarajan, D. Vidyasagar, J. H. Yang, et al., "Bio-Inspired Supramolecular Self-Assembled Carbon Nitride Nanostructures for Photocatalytic Water Splitting," *Advanced Materials* 36, no. 2 (2024): 2306895.

12. M. Fawaz, R. Bahadur, N. Panangattu Dharmarajan, et al., "Emerging Trends of Carbon Nitrides and Their Hybrids for Photo-/Electro-Chemical Energy Applications," *Carbon* 214 (2023): 118345, https://doi.org/10.1016/j.carbon.2023.118345.

13. L. Lin, Z. Yu, and X. Wang, "Crystalline Carbon Nitride Semiconductors for Photocatalytic Water Splitting," *Angewandte Chemie* 131, no. 19 (2019): 6225–6236.

14. C. M. Pelicano and M. Antonietti, "Metal Poly (heptazine imides) as Multifunctional Photocatalysts for Solar Fuel Production," *Angewandte Chemie International Edition* 63, no. 24 (2024): 202406290.

15. Y. Zhou, C. Liao, Y. Fan, et al., "Highly Crystalline Lithium Chloride-Intercalated Graphitic Carbon Nitride Hollow Nanotubes for Effective Lead Removal," *Environmental Science: Nano* 6, no. 11 (2019): 3324–3335.

16. A. Savateev, N. V. Tarakina, V. Strauss, et al., "Potassium Poly (Heptazine Imide): Transition Metal-Free Solid-State Triplet Sensitizer in Cascade Energy Transfer and [3 + 2]-Cycloadditions," *Angewandte Chemie International Edition* 59, no. 35 (2020): 15061–15068.

17. Y. Li, D. Zhang, J. Fan, and Q. Xiang, "Highly Crystalline Carbon Nitride Hollow Spheres with Enhanced Photocatalytic Performance," *Chinese Journal of Catalysis* 42, no. 4 (2021): 627–636.

18. H. Zhuzhang, X. Liang, J. Li, et al., "Precise Manipulation on the Structural Defects of Poly (triazine imide) Single Crystals for Efficient Photocatalytic Overall Water Splitting," *Angewandte Chemie* 137, no. 11 (2025): 202421861.

19. I. F. Teixeira, N. V. Tarakina, I. F. Silva, N. López-Salas, A. Savateev, and M. Antonietti, "Overcoming Electron Transfer Efficiency Bottlenecks for Hydrogen Production in Highly Crystalline Carbon Nitride-Based Materials," *Advanced Sustainable Systems* 6, no. 3 (2022): 2100429.

20. H. Li, G. Zhang, P. Zhang, and H. Mi, "In-Situ One-Step Construction of Poly(heptazine imide)/Poly(triazine imide) Heterojunctions For Photocatalytic Hydrogen Evolution," *Chemsuschem* 17 (2024): 202301849.

21. J. Zhang, X. Liang, C. Zhang, et al., "Improved Charge Separation in Poly(heptazine-triazine) Imides With Semi-Coherent Interfaces for Photocatalytic Hydrogen Evolution," *Angewandte Chemie International Edition* 61, no. 47 (2022): 202210849.

22. L. Lin, Z. Lin, J. Zhang, et al., "Molecular-Level Insights on the Reactive Facet of Carbon Nitride Single Crystals Photocatalysing Overall Water Splitting," *Nature Catalysis* 3, no. 8 (2020): 649–655.

23. G. Zhang, Y. Xu, P. Zhang, C. He, and H. Mi, "Trap-Assisted Exciton Dissociation Through Continuous Trapping/Detrapping in Lithium Ions Inserted Crystalline Carbon Nitride," *Advanced Functional Materials* 34 (2024): 2315116.

24. M. Prabhaharan, A. R. Prabakaran, S. Srinivasan, and S. Gunasekaran, "Density Functional Theory Studies on Molecular Structure, Vibrational Spectra and Electronic Properties of Cyanuric Acid," *Spectrochimica Acta Part A: Molecular and Biomolecular Spectroscopy* 138 (2015): 711–722, https://doi.org/10.1016/j.saa.2014.11.037.

25. T.-E. Chien, K.-L. Li, P.-Y. Lin, and J.-L. Lin, "Infrared Spectroscopic Study of the Adsorption Forms of Cyanuric Acid and Cyanuric Chloride on TiO_2," *Langmuir* 32, no. 21 (2016): 5306–5313.

26. V. Sangeetha, N. Kanagathara, R. Sumathi, N. Sivakumar, and G. Anbalagan, "Spectral and Thermal Degradation of Melamine Cyanurate," *Journal of Materials* 2013, no. 1 (2013): 262094.

27. A. Savateev, D. Dontsova, B. Kurpil, and M. Antonietti, "Highly Crystalline poly(heptazine imides) by Mechanochemical Synthesis For Photooxidation Of Various Organic Substrates Using An Intriguing Electron Acceptor – Elemental Sulfur," *Journal of Catalysis* 350 (2017): 203–211.

28. X. Liang, S. Xue, C. Yang, et al., "The Directional Crystallization Process of Poly (triazine imide) Single Crystals in Molten Salts," *Angewandte Chemie International Edition* 62, no. 14 (2023): 202216434.

29. K. Zhang, C. Liu, Q. Liu, Z. Mo, and D. Zhang, "Salt-Mediated Structural Transformation in Carbon Nitride: From Regulated Atomic Configurations to Enhanced Photocatalysis," *Catalysts* 13, no. 4 (2023): 717.

30. J. Yu, M. Cai, Q. Cheng, et al., "Understanding the Poly (Triazine Imide) Crystals Formation Process: The Conversion from Heptazine to Triazine," *Chemistry – A European Journal* 30, no. 6 (2024): 202302982, https://doi.org/10.1002/chem.202302982.

31. F. Liu, J. Deng, B. Su, et al., "Poly (triazine imide) Crystals for Efficient CO_2 Photoreduction: Surface Pyridine Nitrogen Dominates the Performance," *ACS Catalysis* 15, no. 2 (2025): 1018–1026.

32. G. Zhang, Y. Xu, J. Zhu, et al., "Enhanced Photocatalytic H_2 Production Independent of Exciton Dissociation in Crystalline Carbon Nitride," *Applied Catalysis B: Environmental* 338 (2023): 123049.

33. Z. Yang, L. Li, S. Zeng, et al., "Nanoarchitecture Manipulation by Polycondensation on KCl Crystals toward Crystalline Lamellar Carbon Nitride for Efficient H_2O_2 Photoproduction," *ACS Applied Materials & Interfaces* 15, no. 6 (2023): 8232–8240.

34. G. Zou, Q. Wang, G. Ye, et al., "Copolymerization of Poly (triazine imide) Single Crystal Nanoplates with Enhanced Charge Transfer for Efficient Photocatalytic Overall Water Splitting," *Advanced Functional Materials* 35, no. 28 (2025): 2420899.

35. J. Tauc, R. Grigorovici, and A. Vancu, "Optical Properties and Electronic Structure of Amorphous Germanium," *physica status solidi B* 15, no. 2 (1966): 627–637.

36. E. Güler, Ş. Uğur, M. Güler, and G. Uğur, "Multifunctional Properties of 2D Graphitic Carbon Nitride: A Comprehensive First-Principles Study," *Journal of Inorganic and Organometallic Polymers and Materials* (2026), https://doi.org/10.1007/s10904-025-04097-5.

37. D.-P. Bui, M.-T. Pham, H.-H. Tran, T.-D. Nguyen, T. M. Cao, and V. V. Pham, "Revisiting the Key Optical and Electrical Characteristics in Reporting the Photocatalysis of Semiconductors," *ACS omega* 6, no. 41 (2021): 27379–27386.

38. P. Borlido, T. Aull, A. W. Huran, F. Tran, M. A. Marques, and S. Botti, "Large-Scale Benchmark of Exchange–Correlation Functionals for the Determination of Electronic Band Gaps of Solids," *Journal of chemical theory and computation* 15, no. 9 (2019): 5069–5079.

Supporting Information

Additional supporting information can be found online in the Supporting Information section.

Supporting File: aenm70908-sup-0001-SuppMat.docx.